Article:

Yang, W., Chen, J., Liu, W. orcid.org/0000-0003-2968-2888 et al. (1 more author) (2017) Moving Target Azimuth Velocity Estimation for the MASA Mode Based on Sequential SAR Images. IEEE Journal of Selected Topics in Applied Earth Observations and Remote Sensing, 10 (6). pp. 2780-2790. ISSN 1939-1404

https://doi.org/10.1109/JSTARS.2016.2641744

Moving Target Azimuth Velocity Estimation for the MASA Mode Based on Sequential SAR Images

Wei Yang, Member, IEEE, Jie Chen, Member, IEEE, Wei Liu, Senior Member, IEEE,

Pengbo Wang, Member, IEEE

Abstract—A novel azimuth velocity estimation method is proposed based on the multiple azimuth squint angles (MASA) imaging mode, acquiring sequential SAR images with different squint angles and time lags. The MASA mode acquisition geometry is given first, and the effect of target motion on azimuth offset and slant range offset is discussed in detail. Then, the azimuth velocity estimation accuracy is analyzed, considering the errors caused by registration, defocusing and range velocity. Moreover, the interaction between target azimuth velocity and range velocity is studied for a better understanding of the azimuth velocity estimation error caused by range velocity. With the proposed error compensation step, the new method can achieve a very high accuracy in azimuth velocity estimation, as verified by experimental results based on both simulated data and the TerraSAR-X data.

Index Terms—Synthetic aperture radar (SAR), velocity estimation, multiple azimuth squint angles, sequential images

I. INTRODUCTION

THe rapid development of space-borne synthetic aperture radar (SAR) techniques, such as antenna azimuth pattern steering, allows for innovative applications to meet the rising demand in monitoring, recognition, and classification. By increasing the azimuth pattern steering angle span, several advanced imaging modes, including TOPS, inverse TOPS, sliding spotlight and staring spotlight [1]-[4], have been proposed for a higher geometry resolution or a wider range coverage, and adopted in some advanced SAR satellites, such as ALOS-2 [5], Sentinel-1 [6] and TerraSAR-X [7]. In addition, improved azimuth steering span is also beneficial to moving target detection and velocity estimation. Our research is focused on the innovative imaging mode and the corresponding processing method for moving target azimuth velocity estimation.

Moving target velocity estimation has been studied for a long time in the SAR community. The effects of target motion on position change, resolution distortion and shadow feature were analyzed in [8]-[11], and several classic methods were proposed. For example, by using the information of position change, a velocity estimation method was proposed based on evaluation of the temporal correlation in SAR images [12]. However, the accuracy of this method is poor, and it only works for point-like moving target. Based on resolution distortion caused by target motion, refocusing methods were proposed, such as the shear averaging (SA) method [13] and the method based on the velocity correlation function (VCF) [14], [15]. The SA method is sensitive to azimuth velocity, but incapable of range velocity estimation. Compared with the SA method, the VCF method is more efficient, and can estimate velocity in both azimuth and range directions. Nonetheless, since resolution distortion is normally not obvious enough, it is difficult for both methods to achieve a high accuracy.

With the development of multiple-channel and distributed SAR systems, methods with displacement phase center antenna (DPCA) [16], along track interferometry (ATI) [17] and space time adaptive processing (STAP) [18] were proposed. STAP is the best method in theory, but it needs prior knowledge of clutter and requires a significant amount of computing resources, and therefore becomes impractical in many cases. Compared with STAP, DPCA and ATI are easier to implement with a moderate computation load. However, DPCA is limited by a strict relationship between pulse repetition frequency (PRF) and phase center interval. As for ATI, velocity estimation accuracy can be affected easily by both noise and correlation of the multi-channel data. As a result, the DPCA method is usually used in combination with ATI (short for DPCA-ATI) for improved velocity estimation accuracy [19], [20]. However, DPCA-ATI is only suitable for range velocity estimation, and does not work for the azimuth one.

Regarding azimuth velocity estimation, a novel imaging mode was presented for moving target indication, namely the bidirectional mode (short for BiDi) [21]-[23], which is based on an azimuth beam pattern with two major lobes pointing to different directions simultaneously. As a result, the same area is scanned twice as the sensor passes with a short along track separation in-between the two acquisitions. In the observed area, the position of stationary targets will not change between these two images, but a position offset will be clearly visible for

W. Yang, J. Chen and P. Wang are with the School of Electronic and Information Engineering, Beihang University, Beijing 100191, China. (e-mail: chenjie@buaa.edu.cn)

W. Liu is with the Department of Electronic and Electrical Engineering, University of Sheffield, Sheffield S1 3JD, U.K.

moving target and easy to be detected. However, since signals from different directions are received at the same time, they should be separated in the Doppler spectral domain, which needs a significantly increased PRF. With an increased PRF, the range coverage will become narrow, leading to reduction in observing efficiency. Moreover, the effect of target range velocity on azimuth velocity estimation is ignored, which will lead to a significant estimation error, especially with a high range velocity.

In this paper, a novel azimuth velocity estimation method is proposed, in combination with the multiple azimuth squint angles (MASA) imaging mode. In the MASA mode, the same area will be observed with different azimuth squint angles by employing the azimuth steering technique [24], [25], acquiring sequential SAR images with different time lags. Different from the BiDi mode, the MASA mode receives signals from different azimuth squint angles at different time, and does not need to increase PRF to separate signals in the Doppler frequency domain, leading to a much wider range coverage than the BiDi mode. Moreover, the MASA mode can obtain more than two images, which helps improving the velocity estimation accuracy by an averaging operation. Furthermore, expressions for azimuth estimation errors due to defocusing and range velocity are derived, and compensation methods are provided. The performance of the proposed method is verified by both simulated data and the real TerraSAR-X image data.

This paper is organized as follows. In Sec. II, the MASA mode is introduced, and the target motion effects are analyzed based on acquisition geometry. In Sec. III, the proposed velocity estimation method is given in detail, and azimuth velocity estimation errors are also analyzed, especially with respect to range velocity. Experimental results are provided in Sec. IV, and conclusions are drawn in Sec. V.

II. Multiple Azimuth Squint Angles Imaging

In this section, the MASA mode is introduced based on acquisition geometry. Combined with the MASA mode, target motion effects caused by azimuth velocity and range velocity are analyzed. Moreover, the interaction between azimuth velocity and range velocity is discussed in detail to show its effects on sequential SAR images, providing the theoretical foundation for the velocity estimation method presented in Section III.

A. Acquisition Geometry

Fig. 1 shows the MASA acquisition geometry, taking three observations as an example. In the first observation, from T_1 to T_2, the target area is observed with an azimuth squint angle φ_1, and the moving target position is in P_1. With a time lag $t_{lag1,2}$ and $t_{lag2,3}$, the second and third observations are performed, with azimuth squint angles φ_2 and φ_3, respectively. Correspondingly, the target moves to the positions P_2 and P_3. Three sequential SAR images are acquired by the satellite, with the moving target appearing at different positions. Note that the number of observations is dependent on azimuth steering span. The larger the azimuth steering span is, the more observations we can make for the same area, leading to more accurate estimation results through the averaging operation.

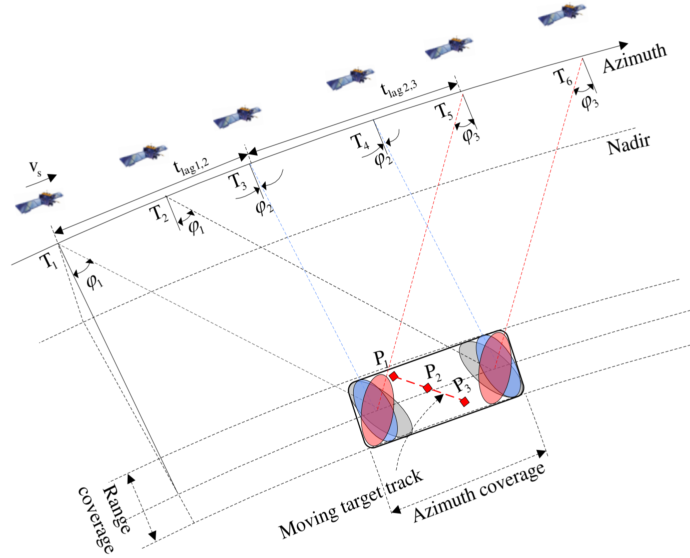

Fig. 1. MASA imaging mode acquisition geometry with three observations.

B. Doppler Characteristic Analysis due to Target Motion

The target motion effect on SAR image has been analyzed before, including the effects on resolution [8], range smear [9], sharpness [13], spectrum shift [20], and so on. However, they are mainly discussed based on boresight acquisition. In the MASA mode, sequential SAR images are acquired with different azimuth squint angles, and the effects will be different. Moreover, in the MASA mode, velocity is estimated by pixel offsets among sequential SAR images, which are affected by the imaging process. Therefore, the effects caused by the image formation process should be taken into account as well. In this part, Doppler characteristics, azimuth time offset and slant range offset are derived in detail, supported by simulation analysis.

In order to avoid significant defocusing, a moderate resolution is usually used for moving target indication in the MASA mode. With moderate resolution, considering a target moving with a constant azimuth velocity v_a and range velocity v_r shown in Fig. 2, the instantaneous slant range variation with time can be written as

$$r(t)=\sqrt{\left(r_0\sin\varphi+v_a t-v_s t\right)^2+\left(r_0\cos\varphi\sin\theta+v_r t\right)^2+\left(r_0\cos\varphi\cos\theta\right)^2} \quad (1)$$

where r_0 is the reference slant range at $t=0$, v_s is radar effective velocity, θ is the elevation angle, φ is the azimuth squint angle, t is the azimuth time. Moreover, the azimuth squint angle is defined to be positive for forward looking, while negative for backward looking. With respect to the boresight, the azimuth squint angle is zero.

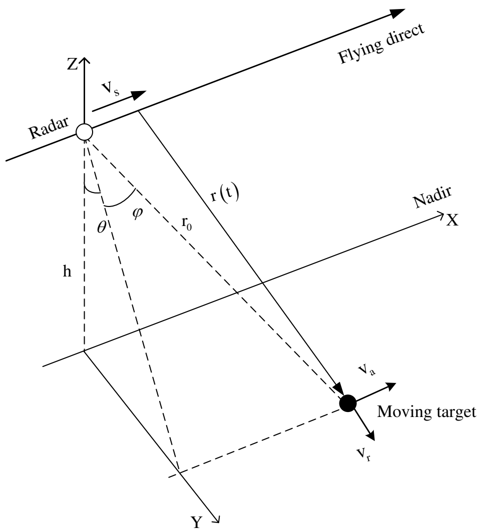

Fig. 2. Geometry model of the moving target.

Based on (1), the Doppler centroid and Doppler frequency modulated rate are derived as follows:

$$f_d = \frac{2}{\lambda}\frac{dr(t)}{dt}\Big|_{t=0} = f_{d0} + \Delta f_d \tag{2}$$

$$f_r = \frac{2}{\lambda}\frac{d^2 r(t)}{dt^2}\Big|_{t=0} = f_{r0} + \Delta f_r \tag{3}$$

where λ is wavelength, f_{d0} and f_{r0} represent the Doppler centroid frequency and Doppler frequency modulated rate of stationary target, and Δf_d and Δf_r are the corresponding variations caused by target motion. We also have

$$f_{d0} = -\frac{2}{\lambda} v_s \sin\varphi \tag{4}$$

$$f_{r0} = \frac{2v_s^2}{\lambda r_0}\cos^2\varphi \tag{5}$$

$$\Delta f_d = \Delta f_{d,v_a} + \Delta f_{d,v_r} \tag{6}$$

$$\Delta f_r = \Delta f_{r,v_a} + \Delta f_{r,v_r} + \Delta f_{r,v_a,v_r} \tag{7}$$

In order to analyze the azimuth and range velocities separately, we define

$$\Delta f_{d,v_a} = \frac{2\sin\varphi}{\lambda} v_a \tag{8a}$$

$$\Delta f_{d,v_r} = \frac{2\sin\theta\cos\varphi}{\lambda} v_r \tag{8b}$$

$$\Delta f_{r,v_a} = \frac{2}{\lambda r_0}\left(-2v_a v_s \cos^2\varphi + v_a^2\cos^2\varphi\right) \approx -\frac{4}{\lambda r_0} v_a v_s \cos^2\varphi \tag{9a}$$

$$\begin{aligned}\Delta f_{r,v_r} &= \frac{2}{\lambda r_0}\left(2v_r v_s \sin\theta\sin\varphi\cos\varphi + v_r^2\cos^2\theta + v_r^2\sin^2\theta\sin^2\varphi\right) \\ &\approx \frac{4}{\lambda r_0} v_r v_s \sin\theta\sin\varphi\cos\varphi\end{aligned} \tag{9b}$$

$$\Delta f_{r,v_a,v_r} = -\frac{4}{\lambda r_0}\left(v_r v_a \sin\theta\sin\varphi\cos\varphi\right) \approx 0 \tag{9c}$$

Based on (8a) and (8b), the Doppler spectrum shift caused by azimuth velocity and range velocity are independent, and it will result in an offset in azimuth. With respect to the Doppler frequency modulated rate variation, $\Delta f_{r,v_a,v_r}$ is basically zero and its effect can be ignored. In the case of small squint angle, compared with $\Delta f_{r,v_r}$, $\Delta f_{r,v_a}$ is the dominant factor in SAR image defocusing.

Fig. 3 shows the peak to peak value of residual quadratic phase error due to target motion, using the parameters listed in Table. I.

TABLE I
SIMULATION PARAMETERS

Parameters	Value
Wavelength	0.03m
Elevation	35.0°
Orbit height	525km
PRF	5000Hz
Aperture time	0.43s
Effective velocity	7500m/s

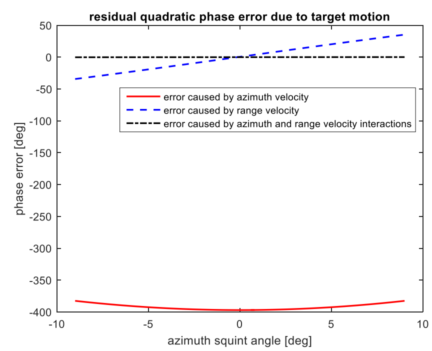

Fig. 3. The peak to peak value of residual quadratic phase error by target motion with 30m/s azimuth velocity and 30m/s range velocity. Azimuth velocity introduces a large quadratic phase error, resulting in significant azimuth resolution deterioration (red solid line). The range velocity results to a small quadratic phase error, whose effects on resolution can be ignored (blue dashed line). Quadratic phase error caused by interactions between azimuth and range velocities is nearly zero (black dashdot line).

As shown in Fig. 3, the Doppler frequency modulated rate variation will lead to image defocusing. When the variation is large enough, pattern distortion of the impulse response function (IRF) will occur, causing a position measurement error. This phenomenon will be discussed in Sec. III.

C. Azimuth Time Offset

Due to the target motions, the Doppler spectrum shift will introduce a time offset in azimuth

$$\Delta t_A = -\frac{\Delta f_d}{f_r} = -\frac{\Delta f_{d,v_a} + \Delta f_{d,v_r}}{f_r} = \Delta t_{A,v_a} + \Delta t_{A,v_r} \tag{10}$$

where $\Delta t_{A,v_a}$ and $\Delta t_{A,v_r}$ are azimuthal time offset caused by v_a and v_r, respectively:

$$\Delta t_{A,v_a} = -\frac{2v_a}{\lambda\cdot f_r}\sin\varphi \approx -\frac{v_a}{v_s^2\cos^2\varphi} r_0 \sin\varphi \tag{11a}$$

$$\Delta t_{A,v_r} = -\frac{2v_r\sin\theta}{\lambda\cdot f_r}\cos\varphi \approx -\frac{v_r}{v_s^2\cos\varphi} r_0 \sin\theta \tag{11b}$$

With the parameters in Table. I, azimuthal time offset caused by $v_a = 10m/s$ and $v_r = 10m/s$ is shown in Fig. 4.

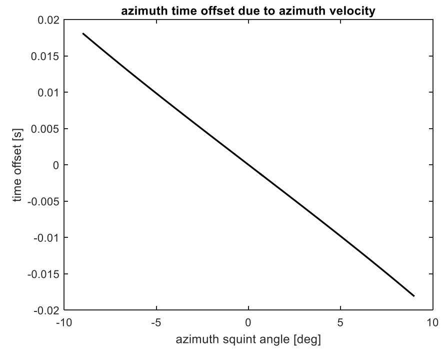

(a) Azimuth time offset caused by azimuth velocity

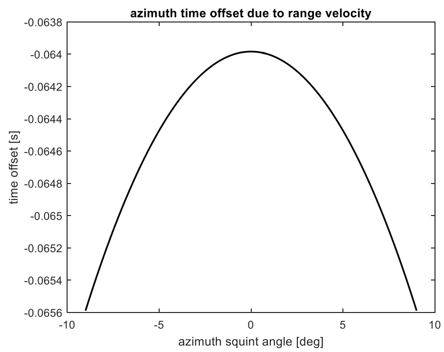

(b) Azimuth time offset caused by range velocity

Fig. 4. Azimuth time offset. (a) azimuth velocity leads to a backward offset in forward looking acquisition, and a forward offset in backward looking acquisition; (b) range velocity leads to a backward offset in both forward and backward looking acquisition.

It can be seen that, azimuth offset caused by range velocity is symmetric, which means forward and backward looking will lead to the same offset with the same absolute value of azimuth squint angle. In contrast to $\Delta t_{A,v_r}$, $\Delta t_{A,v_a}$ is anti-symmetric, and causes a smaller azimuth offset with the same squint angle. However, $\Delta t_{A,v_r}$ varies little with the azimuth squint angle.

D. Slant Range Offset

Target motion also affects range history, causing a slant range offset, which raises two major issues. Firstly, in SAR image, position of the moving target is away from its real positon along the slant range direction. Secondly, the moving target will be located at a wrong range bin. Consequently, mismatched Doppler parameters are used for azimuth compression during the image formation process, which will cause an extra time offset in azimuth.

Because $f_{d0} \gg \Delta f_d$, slant range offset can be approximated as follows:

$$\Delta s_r \approx \frac{\lambda}{2}\left(f_d + \frac{1}{2} f_r \Delta t_A \right)\Delta t_A \approx \frac{\lambda}{2} f_{d0}\Delta t_A \qquad (12)$$

Then, the slant range offsets caused by v_a and v_r are given by

$$\Delta s_{r,v_a} = -\frac{f_{d0}}{f_r} v_a \sin\varphi \approx \frac{v_a}{v_s} r_0 \frac{\sin^2\varphi}{\cos^2\varphi} \qquad (13a)$$

$$\Delta s_{r,v_r} = -\frac{f_{d0}}{f_r} v_r \sin\theta\cos\varphi \approx \frac{v_r}{v_s} r_0 \frac{\sin\varphi}{\cos\varphi}\sin\theta \qquad (13b)$$

Using the parameters in Table. I, slant range offset caused by $v_a = 10\mathrm{m/s}$ and $v_r = 10\mathrm{m/s}$ is shown in Fig. 5.

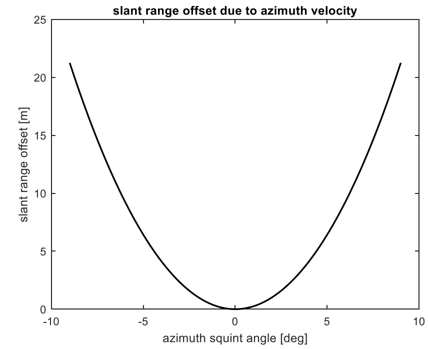

(a) Slant range offset caused by azimuth velocity

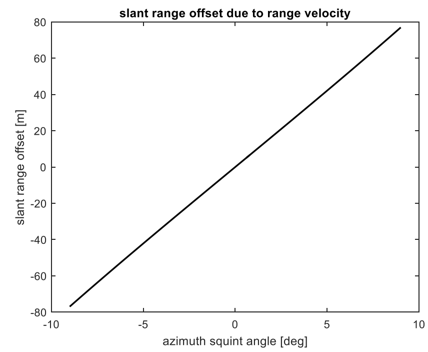

(b) Slant range offset caused by range velocity

Fig. 5. Slant range offset. (a) slant range offset caused by azimuth velocity shows a quadratic increase with azimuth squint angle. (b) slant range offset caused by range velocity varies linearly with azimuth squint angle.

For the azimuth velocity effect on slant range offset, it shows a quadratic increase with azimuth squint angle, leading to the same slant range offset in forward looking and backward looking acquisition, with the absolute value of the same squint angle. However, range velocity varies linearly, and it introduces a significantly larger slant range offset compared with azimuth velocity.

Moreover, slant range offset caused by target velocity leads to range bin variation. For example, assuming range bin $p_r = c/2/f_s$ is equal to 2m. According to the parameters listed in Table. I, the resultant range bin variation is analyzed and shown in Fig. 6.

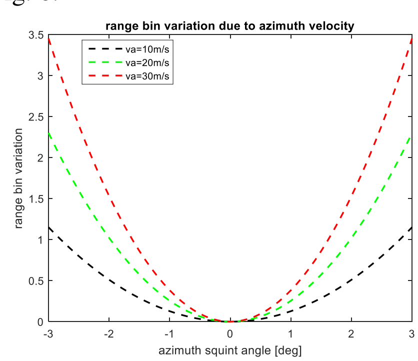

(a) Slant range offset caused by azimuth velocity

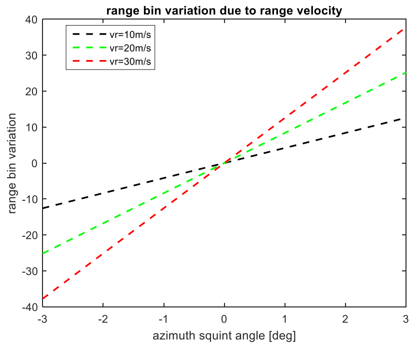

(b) Slant range offset caused by range velocity

Fig. 6. Slant range offset on the variation of range bins. (a) Slant range offset caused by azimuth velocity leads to one range bin variation with squint angle 2.8°, 2.0° and 1.6° corresponding azimuth velocity 10m/s, 20m/s and 30m/s; (b) With respect to range velocity, one range bin variation will occur with squint angle 0.24°, 0.12° and 0.08°, corresponding to range velocity 10m/s, 20m/s and 30m/s, respectively.

Regarding azimuth velocity, with the azimuth squint angle $\varphi = 3^{\circ}$, it causes only one, two and three range bin variations, corresponding to $v_a = 10\mathrm{m/s}$, $v_a = 20\mathrm{m/s}$ and $v_a = 30\mathrm{m/s}$. However, with respect to range velocity, it will lead to the change of dozens of range bins. As a consequence, mismatched Doppler parameters are used in image formation process, resulting in a noticeable azimuth time offset and the corresponding azimuth velocity estimation error.

III. Velocity Estimation

In this section, the proposed azimuth velocity estimation method is provided in detail based on the MASA mode. Its performance is analyzed by considering different factors including range velocity, registration and defocusing.

A. The Proposed Method and Range Velocity Effects

Azimuth time offset is determined by the Doppler centroid frequency shift [26]. The azimuth pixel offset Δn_a can be obtained by

$$\Delta n_a \cdot \Delta t_s = -\frac{\Delta f_{d,total}}{f_r} = -\frac{\Delta f_{d,v_a} + \Delta f_{d,v_r} + \Delta f_{d,mis,v_r} + \Delta f_{d,mis,v_a}}{f_r} \quad (14)$$

where Δt_s is the pixel sampling time interval and $\Delta f_{d,total}$ is the total Doppler centroid frequency shift. $\Delta f_{d,total}$ is composed of four parts, including $\Delta f_{d,v_a}$ (caused by azimuth velocity), $\Delta f_{d,v_r}$ (caused by range velocity), $\Delta f_{d,mis,v_a}$ (caused by parameter mismatch due to azimuth velocity) and $\Delta f_{d,mis,v_r}$ (caused by parameter mismatch due to range velocity).

According to (14), since azimuth pixel offsets are determined by both azimuth and range velocities, it is impossible to estimate target velocity using azimuth pixel offsets with a single SAR image. Fortunately, we can employ sequential SAR images for target motion estimation by using the difference of azimuth pixel offset. However, challenge arises in the separation of effects of azimuth velocity and range velocity.

First, we analyze the effects caused by range velocity and Doppler parameter mismatch on azimuth velocity estimation, deriving the differentiations of $\Delta f_{d,v_r}$, $\Delta f_{d,mis,v_r}$ and $\Delta f_{d,mis,v_a}$ as follows (see Appendix).

$$\begin{aligned} d\left[\Delta f_{d,v_r}\right] &= \frac{\partial \Delta f_{d,v_r}}{\partial \varphi} d\varphi + \frac{\partial \Delta f_{d,v_r}}{\partial \theta} d\theta \\ &= -\frac{2v_r}{\lambda}\sin\theta\sin\varphi\Delta\varphi + \frac{2v_r}{\lambda}\cos\theta\cos\varphi\Delta\theta \end{aligned} \quad (15)$$

$$\begin{aligned} d\left[\Delta f_{d,mis,v_r}\right] &= \frac{\partial \Delta f_{d,mis,v_r}}{\partial r}\frac{\partial r}{\partial \varphi} + \frac{\partial \Delta f_{d,mis,v_r}}{\partial r}\frac{\partial r}{\partial \theta} \\ &\approx \frac{2v_r}{\lambda}\sin\theta\sin\varphi\Delta\varphi + \frac{2v_r}{\lambda}\cos\theta\frac{\sin^2\varphi}{\cos\varphi}\Delta\theta \end{aligned} \quad (16)$$

$$d\left[\Delta f_{d,mis,v_a}\right] = \frac{\partial \Delta f_{d,mis,v_a}}{\partial r}\frac{\partial r}{\partial \varphi} = \frac{4v_a}{\lambda}\frac{\sin^2\varphi}{\cos^3\varphi}\Delta\varphi \approx 0 \quad (17)$$

where $\Delta\varphi$ and $\Delta\theta$ are the difference of azimuth squint angles and elevation angles of two arbitrary acquisitions.

Regarding the differentiation of $\Delta f_{d,mis,v_a}$, it is very small. As shown in Fig. 6, it cannot even cause a range bin variation with small squint angle acquisition. Moreover, the effect can be cancelled by choosing two images with the squint angle φ and $-\varphi$. As a result, Doppler parameter mismatch caused by azimuth can be ignored.

As for range velocity, it will cause azimuth velocity estimation errors. Adding (15) and (16) together, we can obtain the residual Doppler centroid frequency shift, given by

$$\Theta_{v_r \to v_a} = \frac{2v_r}{\lambda}\cos\theta\cos\varphi\Delta\theta + \frac{2v_r}{\lambda}\cos\theta\frac{\sin^2\varphi}{\cos\varphi}\Delta\theta = \frac{2v_r}{\lambda}\frac{\cos\theta}{\cos\varphi}\Delta\theta \quad (18)$$

For details of the proposed velocity estimation method, we consider two arbitrary SAR images S_i and S_j, with squint angles φ_i and φ_j, respectively. As shown in Fig. 7, we can obtain the following equation.

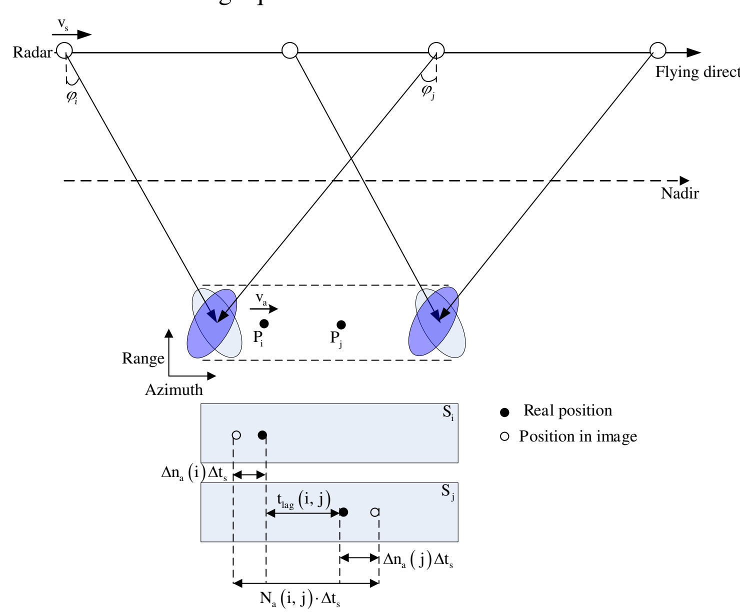

Fig. 7. Azimuth time offset between two acquisitions with azimuth squint angles φ_i and φ_j. Azimuth time offset is composed of three parts, including time offset in every image and time lag between two acquisitions.

$$N_a(i,j)\cdot\Delta t_s = \Delta n_a(i)\Delta t_s - \Delta n_a(j)\Delta t_s + t_{lag}(i,j) \quad (19)$$

where $N_a(i,j)$ is the difference of pixel offset between S_i and S_j in azimuth, and $t_{lag}(i,j)$ is the time lag between two acquisitions.

$$\Delta t_{lag}(i,j) \approx \frac{r_i \sin\varphi_i}{v_s^2} v_a - \frac{r_j \sin\varphi_j}{v_s^2} v_a \quad (20)$$

Substituting (14) and (20) into (19), we have

$$\begin{aligned} N_a(i,j)\Delta t_s &= \Delta n_a(j)\Delta t_s - \Delta n_a(i)\Delta t_s + \Delta t_{lag}(i,j) \\ &= v_a\left[\frac{r_i}{v_s^2}\frac{\sin\varphi_i\left(1+\cos^2\varphi_i\right)}{\cos^2\varphi_i} - \frac{r_j}{v_s^2}\frac{\sin\varphi_j\left(1+\cos^2\varphi_j\right)}{\cos^2\varphi_j}\right] + \frac{\Theta_{v_r\to v_a}}{f_r} \end{aligned} \quad (21)$$

Then, the azimuth velocity estimation result and the corresponding estimation error are given by

$$\hat{v}_a(i,j) = \frac{v_s^2\cdot N_a(i,j)\cdot\Delta t_s}{\left[\frac{r_i\sin\varphi_i\left(1+\cos^2\varphi_i\right)}{\cos^2\varphi_i} - \frac{r_j\sin\varphi_j\left(1+\cos^2\varphi_j\right)}{\cos^2\varphi_j}\right]} \quad (22)$$

$$\hat{v}_{a,error}(i,j) = -\frac{v_r r_i \cos\theta_i \Delta\theta}{\cos^3\varphi_i\left[\frac{r_i\sin\varphi_i\left(1+\cos^2\varphi_i\right)}{\cos^2\varphi_i} - \frac{r_j\sin\varphi_j\left(1+\cos^2\varphi_j\right)}{\cos^2\varphi_j}\right]} \quad (23)$$

If we choose two acquisitions with the azimuth squint angles $-\varphi_i$ and φ_i, $\hat{v}_a(i,j)$ and $\hat{v}_{a,error}(i,j)$ can be rewritten as:

$$\hat{v}_a(-i,i) = \frac{v_s^2\cdot N_a(i,j)\cdot\Delta t_s\cdot\cos^2\varphi}{2r\sin\varphi\left(1+\cos^2\varphi\right)} \quad (24)$$

$$\hat{v}_{a,error}(-i,i) \approx -\frac{\cos\theta\cdot\Delta\theta}{\sin 2\varphi\left(1+\cos^2\varphi\right)}\cdot v_r \quad (25)$$

The estimation error due to v_r is shown in Fig.8. So, in order to obtain an accurate azimuth velocity estimation result, the error caused by range velocity should be compensated, especially for the case with a small azimuth velocity and a large range velocity.

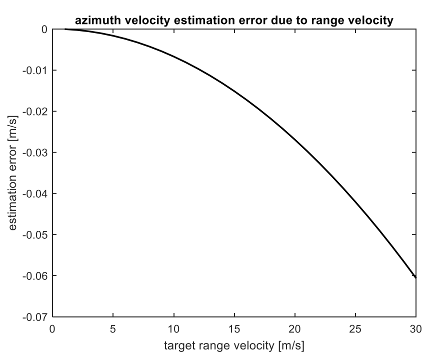

Fig. 8. Azimuth velocity estimation error change with range velocity from 0m/s to 30m/s using two images, with azimuth squint angles $\varphi = -3^{o}$ and $\varphi = 3^{o}$.

B. Registration Effect on Azimuth Velocity Estimation

Image registration error has direct influence on azimuth velocity estimation accuracy. In order to illustrate the effect due to one pixel registration error, using the parameters listed in Table. I, we choose ten different combinations of two images. One image is acquired with the azimuth squint angle -5°, and the other one with the azimuth squint angle varying from -4° to 5°.

As shown in Fig. 9, a larger difference in squint angle or a longer time lag is needed for reducing the effect caused by image registration error. Assuming the registration error is random, it can be reduced by calculating the expectation of $\hat{v}_a(i,j)$.

$$\hat{v}_a = E\left[\hat{v}_a(i,j)\right] \approx \frac{\sum_{i=1}^{n}\sum_{j=i+1}^{n}\hat{v}_a(i,j)}{C_n^2} \quad (26)$$

where n is the number of sequential SAR images, $E[\cdot]$ is the expectation operation and C denotes the combination operation.

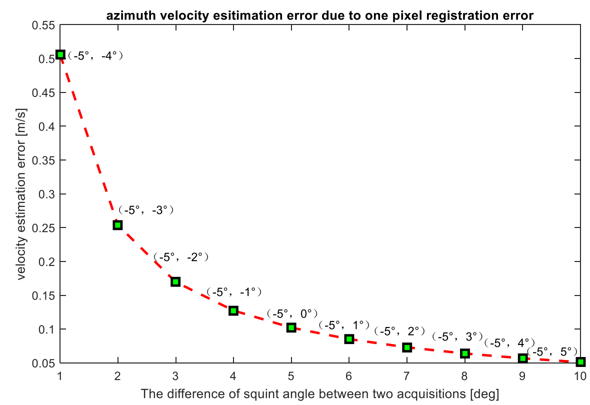

Fig. 9. Azimuth velocity estimation error due to one pixel registration error. Ten different combinations of two images are selected, with the difference of squint angle from 1° to 10 °, which introduces an azimuth velocity error from 0.05m/s~0.5m/s.

C. Defocusing Effect on Azimuth Velocity Estimation

As mentioned in Sec. II, target motion in azimuth is the major factor for defocusing, due to large residual phase error caused by it. When the phase error is large enough, pattern distortion of IRF will occur. As shown in Fig. 10, when residual phase error reaches 1.5π, the main lobe is cut into two parts. Consequently, the image will become blurry, leading to possible position measurement error.

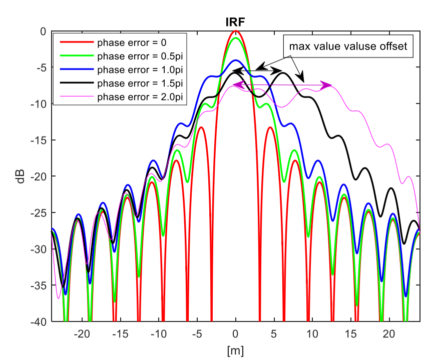

Fig. 10. Azimuth velocity estimation error due to defocusing. Residual phase error not only causes loss in gain, but also pattern distortion. And, the position of maximum value will change, leading a position measurement error.

In order to mitigate the effect of defocusing, a refocusing operation is adopted for fast moving target detection and velocity estimation. Taking 1.5π as the judgment threshold value,

$$\left|\pi\Delta f_{r,v_a}\left(\frac{T}{2}\right)^2\right| = \left|\pi\frac{1}{\lambda r_0}v_a v_s \cos^2\varphi \frac{v_s}{\rho_a f_{r0}}T\right| < 1.5\pi \qquad (27)$$

Then,

$$v_{a,threshold} < 3\frac{p_a}{T}$$

where p_a is azimuth resolution, and T is synthetic aperture time. It means that target movement cannot exceed 3 time of ρ_a during the synthetic aperture time; otherwise, there will be a significant pattern distortion, resulting in an error of nearly three pixels. However, in the case of low signal-to-clutter ratio (SCR), due to the gain loss of moving target, the background clutter may have noticeable effect on pixel offset measurement. So, a smaller judgment threshold value should be used according to the SCR.

If the estimated azimuth velocity result is larger than $v_{a,threshold}$, a refocusing operation for moving target is required by transforming the image into the Doppler domain, using the phase compensation function

$$\Omega(f_a) = \exp\left\{\pi f_a^2 \frac{\Delta f_{r,v_a}}{f_{r0}\left(f_{r0}+\Delta f_{r,v_a}\right)}\right\} = \exp\left\{-2\pi\frac{\hat{v}_a}{v_s}\frac{f_a^2}{f_{r0}+\Delta f_{r,v_a}}\right\} \qquad (28)$$

where f_a is azimuth frequency. After phase compensation, the azimuth velocity estimation method is implemented again for a more accurate value.

The flowchart of the proposed method is shown in Fig. 11, where the classic chirp scaling approach is adopted [27], for focusing targets at their corresponding closest slant ranges.

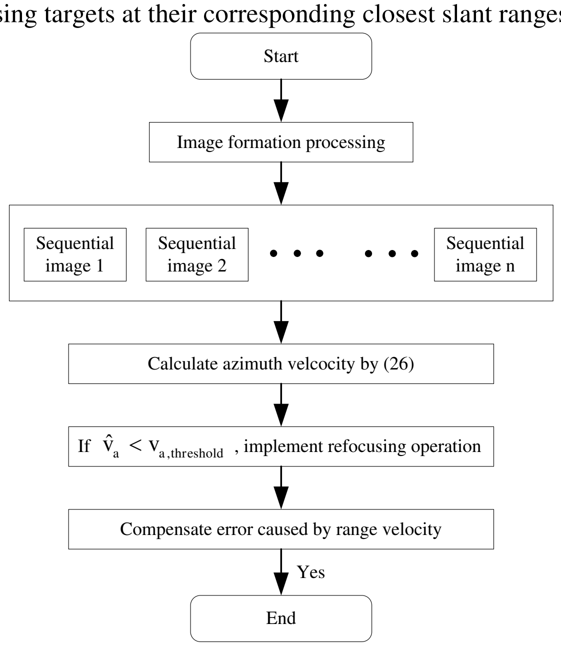

Fig. 11. Flowchart of the proposed azimuth velocity estimation method.

IV. EXPERIMENTAL RESULTS

A. Results with Simulated Data

Experiments are performed first by simulation data, with parameters listed in Table. I. Five sequential images are used, with the azimuth angles -5°, -3°, 0°, 3° and 5°. So, ten different combinations ($C_5^2 = 10$) can be used for velocity estimation, and the mean value is used in the following analysis.

Fig. 12 shows the azimuth velocity estimation results with respect to real azimuth velocity from 1m/s to 30m/s and range velocity is 0m/s. With $p_a = 3m$ and $T = 0.43s$, $v_{a,threshold}$ is 21m/s according to (27). Consequently, when azimuth velocity is up to 22m/s, it leads to 0.4m/s estimation error due to pattern distortion. After defocusing compensation, the azimuth velocity estimation accuracy is significantly improved, with an error within 0.08m/s at azimuth velocity 30m/s.

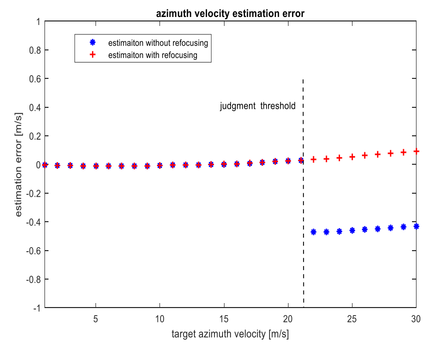

Fig. 12. Azimuth velocity estimation error due to defocusing.

In addition to defocusing, range velocity also has direct influence on azimuth velocity estimation accuracy, especially in case of relatively larger range velocity compared with azimuth velocity. Fig. 13 shows the azimuth velocity estimation error, with range velocity varying from 1m/s to 30m/s. The larger the range velocity is, the greater the estimation error is. When range velocity is up to 30m/s, it results in an estimation error of nearly 0.1 m/s.

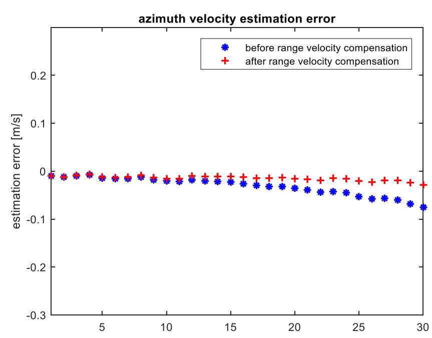

Fig. 13. Azimuth velocity estimation error due to range velocity.

As can be seen from the above simulation results, a more accurate estimation can be obtained by the proposed method, especially by compensating the error due to defocusing and the range velocity effect.

B. Results with TerraSAR-X Staring Spotlight Data

In order to further verify the proposed method, the TerraSAR-X staring spotlight data is utilized, which has an azimuth resolution of 0.25m, with a large azimuth steering span of -2.2°~2.2° [4], [7]. The staring spotlight image is transformed into the Doppler domain, and the valid azimuth frequency spectrum is divided into n sub-spectrums. Since the azimuth frequency coincides with the azimuth squint angle, each sub-spectrum corresponds to the image acquired with different azimuth squint angles. So, sequential SAR images can be obtained by applying Inverse Fast Fourier Transform (IFFT) on each sub-spectrum, as shown in Fig. 14.

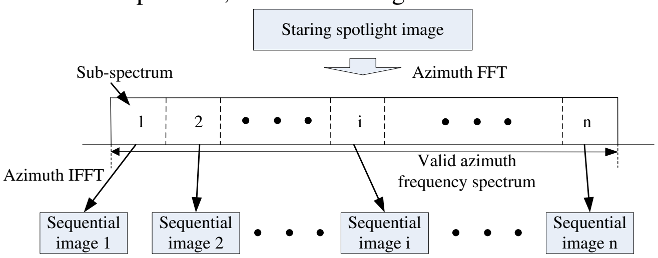

Fig. 14. Sequential images generation using the staring spotlight image.

As shown in Fig. 15, the Shenyangbei railway station staring spotlight image is used, and the parameters are listed in Table. Ⅱ.

TABLE Ⅱ
TERRASAR-X SHENYANGBEI STARING IMAGE PARAMETERS

Image Parameters	
Wavelength	0.031 m
Incidence angle	24.07°
Orbit height	514 km
PRF	4998.45 Hz
Signal sampling rate	329.6 MHz
Scene center slant range	558.470 km
Slant Range Resolution	0.588 m
Azimuth Resolution	0.23 m
Image azimuth sampling rate	42400 Hz
Processing Parameters	
Elevation	22.18°
Effective velocity	7337 m/s
Azimuth valid frequency	32236 Hz
Number of sequential images	5
Squint angel of sequential images	-1.56°, -0.78°, 0°, 0.78°, 1.56°
Time lags between sequential 1 and sequential 5	4.14 s
Sub-image azimuth sampling rate	6448 Hz
Slant range spacing	0.455 m
Azimuth spacing	1.138 m

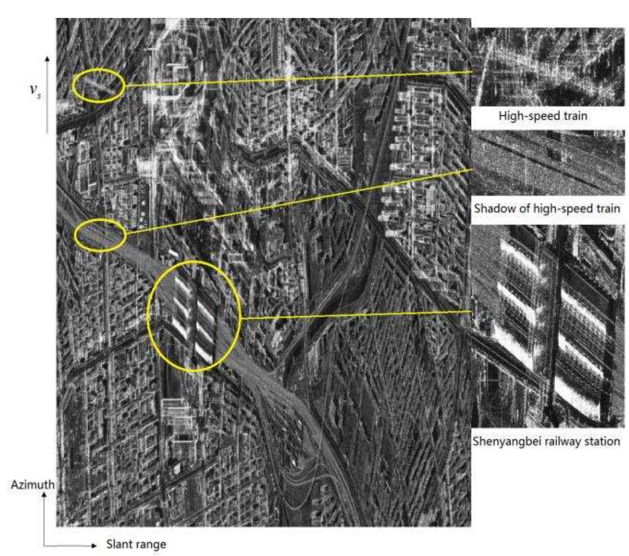

Fig. 15. The TerraSAR-X Shenyangbei railway station staring spotlight image. A high-speed train is moving from right to left, causing a pixel offset in azimuth. The shadow indicates the real position of high-speed train.

In Fig. 15, a high-speed train is moving, and the shadow represents its real position. The shadow movement is clearly visible and can be measured to calculate the velocity as the real velocity of the train. Fig. 16 shows the pixel offset of the shadow in following images. The velocity of shadow is calculated according to the pixel offset, slant range spacing, azimuth spacing and time lag, and the result for azimuth velocity is 2.124 m/s, slant range velocity is -7.028 m/s and the range velocity is -17.227 m/s.

Fig. 17 shows the high-speed train pixel offset in the sequential SAR images, with 15 pixel offset in azimuth. Taking this azimuth offset into (22), the azimuth velocity estimation result is 2.057 m/s. Moreover, considering the range velocity effect that causes a 0.041 m/s error, the modified estimation is 2.098 m/s, which is almost the same as the value calculated according to shadow movement, again verifying the effectiveness of the proposed method.

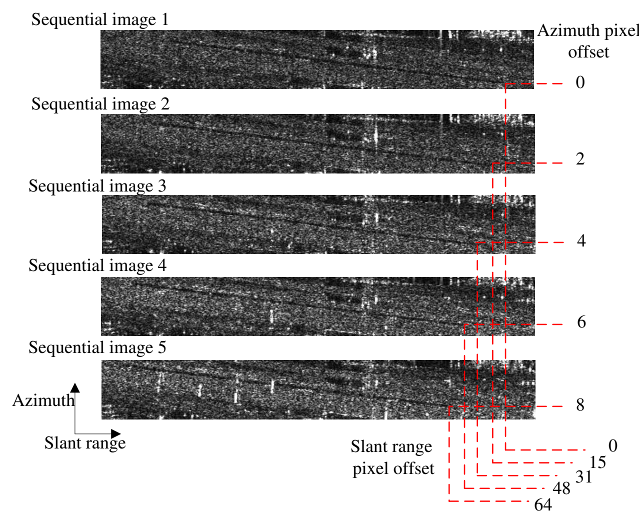

Fig. 16. Shadow pixel offset in sequential images, taking image 1 as the benchmark with 0 pixel offset, and calculating the pixels in slant range and azimuth respectively.

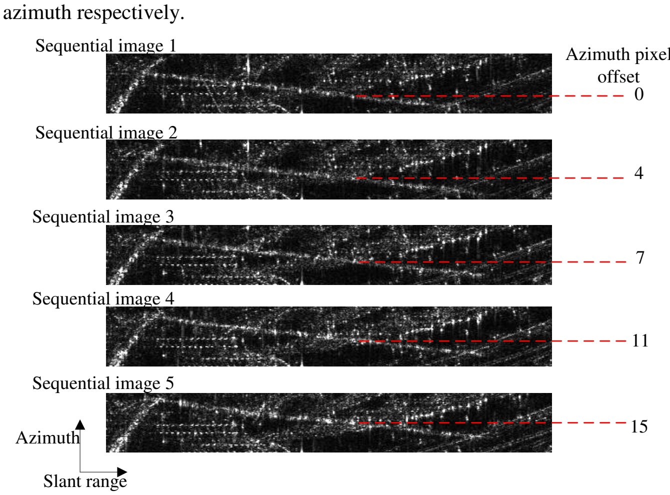

Fig. 17. High-speed offset in sequential images, with 15 pixels in azimuth.

V. CONCLUSION

In this paper, an effective azimuth velocity estimation method has been proposed based on the MASA imaging mode. Combined with the acquisition geometry of the MASA mode, target motion effects were analyzed in detail, including the azimuth offset and slant range offset. Based on the slant range offset, the effect of Doppler parameters mismatch during the image formation process was also discussed. The estimation error was studied considering factors including registration, defocusing and range velocity, with compensation methods presented to improve the accuracy. The effectiveness of the proposed method was demonstrated by experimental results using both simulated data and the TerraSAR-X data. However, due to target motion, moving target will be focused at a wrong position in a SAR image. For example, a moving car may be overlapped with its nearby buildings in the image. If the intensity of background clutter is close to or even stronger than that of the moving target, it would be difficult to obtain the required accurate pixel offsets, resulting in degradation of azimuth velocity estimation accuracy. In order to overcome this problem, clutter suppression techniques can be employed as a topic of future research, but it is beyond the scope of this paper.

APPENDIX

The derivation of equations (16) and (17) is given in detail in the following.

As shown in Fig. 18, the Doppler centroid frequency is given by

$$f_{d0} = -\frac{2v_s}{\lambda}\sin\varphi = -\frac{2v_s}{\lambda}\frac{X_0}{r_0} \tag{A1}$$

The differentiation of f_{d0} is

$$\begin{aligned} d\left[f_{d0}\right] &= -\frac{2v_s}{\lambda}X_0\left(-\frac{1}{r_0^2}\right)dr \\ &= -\frac{2v_s}{\lambda}\frac{X_0}{r_0}\left(-\frac{1}{r_0}\right)dr = -\frac{f_{d0}}{r_0}dr \end{aligned} \tag{A2}$$

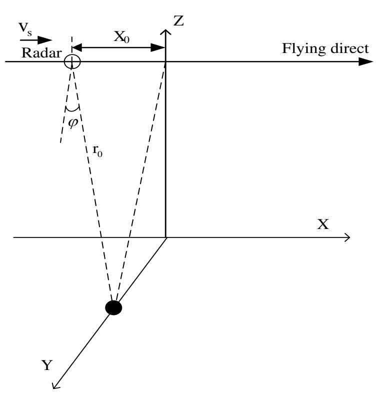

Fig. 18. Acquisition geometry model.

Since $\Delta s_{r,v_r}$ is the function of φ and θ, we can calculate the differentiation of $\Delta f_{d,mis,v_r}$ according to (A2),

$$d\left[\Delta f_{d,mis,v_r}\right] = \frac{\partial \Delta f_{d,mis,v_r}}{\partial r}\frac{\partial r}{\partial \varphi} + \frac{\partial \Delta f_{d,mis,v_r}}{\partial r}\frac{\partial r}{\partial \theta} \tag{A3}$$

Substituting (A2) and (13b) into (A3), we have

$$\begin{aligned} d\left[\Delta f_{d,mis,v_r}\right] &= -\frac{f_{d0}}{r_0}\cdot\left(\frac{\partial \Delta s_{r,v_r}}{\partial\varphi}\right) - \frac{f_{d0}}{r_0}\cdot\left(\frac{\partial \Delta s_{r,v_r}}{\partial\theta}\right) \\ &= -\frac{f_{d0}}{r_0}\cdot\left(\frac{v_r}{v_s}r_0\frac{\sin\theta}{\cos^2\varphi}\right)\Delta\varphi - \frac{f_{d0}}{r_0}\cdot\left(\frac{v_r}{v_s}r_0\frac{\sin\varphi}{\cos\varphi}\cos\theta\right)\Delta\theta \\ &= \frac{2v_s}{\lambda r_0}\sin\varphi\cdot\left(\frac{v_r}{v_s}r_0\frac{\sin\theta}{\cos^2\varphi}\right)\Delta\varphi + \frac{2v_s}{\lambda r_0}\sin\varphi\cdot\left(\frac{v_r}{v_s}r_0\frac{\sin\varphi}{\cos\varphi}\cos\theta\right)\Delta\theta \\ &= \frac{2v_r}{\lambda}\sin\theta\frac{\sin\varphi}{\cos^2\varphi}\Delta\varphi + \frac{2v_r}{\lambda}\cos\theta\frac{\sin^2\varphi}{\cos\varphi}\Delta\theta \end{aligned} \tag{A4}$$

Since φ is small, (A4) can be approximated as follows

$$d\left[\Delta f_{d,mis,v_r}\right] \approx \frac{2v_r}{\lambda}\sin\theta\sin\varphi\Delta\varphi + \frac{2v_r}{\lambda}\cos\theta\frac{\sin^2\varphi}{\cos\varphi}\Delta\theta \tag{A5}$$

As for $\Delta s_{r,v_a}$, it is only a function of φ. So the differentiation of $\Delta f_{d,mis,v_a}$ is given by

$$d\left[\Delta f_{d,mis,v_a}\right] = \frac{\partial \Delta f_{d,mis,v_a}}{\partial r}\frac{\partial r}{\partial\varphi} \tag{A6}$$

In the same way, substituting (A2) and (13a) into (A6), we have

$$\begin{aligned} d\left[\Delta f_{d,mis,v_a}\right] &= -\frac{f_{d0}}{r_0}\cdot\left(\frac{\partial \Delta s_{r,v_a}}{\partial\varphi}\right) = -\frac{f_{d0}}{r_0}\cdot\left(\frac{v_a}{v_s}r_0\frac{2\sin\varphi}{\cos^3\varphi}\right)\Delta\varphi \\ &= \frac{2v_s}{\lambda r_0}\sin\varphi\cdot\left(\frac{v_a}{v_s}r_0\frac{2\sin\varphi}{\cos^3\varphi}\right)\Delta\varphi \\ &= \frac{4v_a}{\lambda}\frac{\sin^2\varphi}{\cos^3\varphi}\Delta\varphi \approx 0 \end{aligned} \tag{A7}$$

ACKNOWLEDGMENT

This work was supported by National Natural Science Foundation of China (NSFC) under Grant No.61132006 and National Natural Science Foundation of China (NSFC) under Grant No. 61171123.

REFERENCES

[1] F. D. Zan, and A. M. Guarnieri, "TOPSAR: Terrain observation by progressive scans," IEEE Trans. Geosci. Remote Sens., vol. 44, no. 9, pp. 2352-2360, Sep. 2006.

[2] A. Meta, J. Mittermayer, P. Prats, R. Scheiber, and U. Steinbrecher, "TOPS imaging with TerraSAR-X: mode design and performance analysis," IEEE Trans. Geosci. Remote Sens., vol. 48, no. 2, pp. 759-769, Feb. 2010.

[3] H. Kuang, J. Chen, and W. Yang, "A modified chirp-scaling algorithm for spaceborne squinted sliding spotlight SAR data processing," in Proc. APSAR, Singapore, Sep. 2015, pp. 459-461.

[4] J. Mittermayer, S. Wollstadt, P. Prats, and R. Scheiber, "The TerraSAR-X staring spotlight mode concept," IEEE Trans. Geosci. Remote Sens., vol. 52, no. 6, pp. 3695-3706, Jun. 2014.

[5] Y. Kankaku, S. Suzuki, and Y. Osawa, "ALOS-2 mission and development status," in Proc. IEEE Int. Geosci. Remote Sens. Symp., Melbourne, Australia, Jul. 2013, pp. 2396-2403.

[6] N. Y. Martinez, P. Prats, F. R. Gonzalez, R. Brcic, R. Shau, D. Geudtner, M. Eineder, and R. Bamler, "Interferometric processing of sentinel-1 TOPS data," IEEE Trans. Geosci. Remote Sens., vol. 54, no. 4, pp. 2220-2234, Apr. 2016.

[7] T. Kraus, B. Bräutigam, J. Mittermayer, S. Wollstadt, and C. Grigorov, "TerraSAR-X staring spotlight mode optimization and global performance predictions," IEEE Journal of Seleted Topics in Applied Earth Observation and Remote Sensing, vol. 9, no. 3, pp. 1015-1027, Mar. 2016.
[8] K. A. Garf, and H. Guthart, "Velocity effects in synthetic apertures," IEEE Trans. Antennas Propag., vol. 17, no. 5, pp. 541-546, Sep. 1969.
[9] R. K. Raney, "Synthetic aperture imaging radar and moving targets," IEEE Trans. Aerosp. Electron. Syst, vol. 7, no. 3, pp. 499-505, May 1971.
[10] K. Ouchi, "On the multilook images of moving targets by synthetic aperture radars," IEEE Trans. Antennas Propag., vol. 33, no. 8, pp. 823-827, Aug. 1985.
[11] H. J. Xu, Z. W. Yang, G. Z. Chen, G. S. Liao, and M. Tian, "A ground moving target detection approach based on shadow feature with multichannel high-resolution synthetic aperture radar," IEEE Geosci. Remote Sens. Lett., vol. 13, no. 10, pp. 1572-1576, Oct. 2016.
[12] M. Kirscht, S. Suzuki, and Y. Osawa, "Detection and velocity estimation of moving objects in a sequence of single-Look SAR images," in Proc. IEEE Int. Geosci. Remote Sens. Symp., Lincoln, USA, May 1996, pp. 333-335.
[13] J. R. Fienup, "Detecting moving targets in SAR imagery by focusing," IEEE Trans. Aerosp. Electron. Syst, vol. 37, no. 3, pp. 794-809, Jul. 2001.
[14] M. Arii, "Efficient motion compensation of SAR imagery by refocusing approach," in Proc. APSAR, Tsukuba, Sep. 2013, pp. 150-151.
[15] M. Arii, "Efficient motion compensation of a moving object on SAR imagery based on velocity correlation function," IEEE Trans. Geosci. Remote Sens., vol. 52, no. 2, pp. 936-946, Feb. 2014.
[16] D. C. Maori, and I. Sikaneta, "A generalization of DPCA preprocess for multichannel SAR/GMTI radars," IEEE Trans. Geosci. Remote Sens., vol. 51, no. 1, pp. 560-572, Jan. 2013.
[17] S. Suchandt, H. Runge, H. Breit, U. Steinbrecher, A. Kotenkov and U. Balss, "Automatic extraction of traffic flows using TerraSAR-X along-track interferometry," IEEE Trans. Geosci. Remote Sens., vol. 48, no. 2, pp. 807-819, Feb. 2010.
[18] L. Rosenberg, and D. A. Gray, "Constrained fast-time STAP for interference suppression in multichannel SAR," IEEE Trans. Aerosp. Electron. Syst, vol. 49, no. 3, pp. 1792-1805, Jul. 2013.
[19] D. Cerutti-Maori, and I. Sikaneta, "Optimum GMTI processing for space-based SAR/GMTI systems - theoretical derivation," in Proc. EUSAR, Aachen, Germany, Jun. 2010, pp. 393-390.
[20] X. Yang, and J. F. Wang, "GMTI based on a combination of DPCA and ATI," in Proc. IET Radar conference, HangZhou, China, Oct. 2015, pp. 1-5.
[21] J. Mittermayer and S. Wollstadt, "Simultaneous bi-directional SAR acquisition with TerraSAR-X," in Proc. EUSAR, Aachen, Germany, Jun. 2010, pp. 732-735.
[22] J. Mittermayer, P. Prats, S. Wollstadt, S. Baumgartner, P. Lopez-Dekker, A. Broquetas, E. M. Varona, G. Krieger, and A. Moreira, "Approach to velocity and acceleration measurement in the bi-directional SAR imaging mode," in Proc. IEEE Int. Geosci. Remote Sens. Symp., Munich, Germany, Jul. 2012, pp. 5618-5621.
[23] J. Mittermayer, S. Wollstadt, P. Prats, P. López-Dekker, G. Krieger, and A. Moreira, "Bidirectional SAR imaging mode," IEEE Trans. Geosci. Remote Sens., vol. 51, no. 1, pp. 807-819, Jan. 2013.
[24] J. Janoth, I. GmbH, S. Gantert, W. Koppe, A. Kaptein, and C. Fischer, "TerraSAR-X2 - Mission overview," in Proc. IEEE Int. Geosci. Remote Sens. Symp., Munich, Germany, Jul. 2012, pp. 22-27.
[25] C. Heer, and C. Schaefer, "TerraSAR-X next generation: Technology aspects," in Proc. APSAR, Seoul, Korea, Sep. 2011, pp. 1-4.
[26] I. G. Cumming, F. H. Wong, "Digital processing of synthetic aperture radar data: algorithms and implementation," Boston: Artech House; 2005.
[27] R. K. Raney, H. Runge, R. Bamler, I. G. Cumming, and F. H. Wang, "Precision SAR processing using chirp scaling," IEEE Trans. Geosci. Remote Sens., vol. 32, no. 4, pp. 786-799, Jul. 1994.

Wei Yang was born in Hubei province, China, in 1983. He received the M.S. and Ph.D. degrees in signal and information processing from Beihang University (BUAA), China, in 2008 and 2011, respectively. In 2005, he studied the inner calibration signal analysis in SAR system. From 2006 to 2010, he focused on the system performance analysis and signal processing of high resolution and wide swath mode in spaceborne SAR. From 2011 to 2013, he is a postdoctoral in the School of Electronics and Information Engineering, Beihang University. Since July 2013, he has been with the school of Electronics and Information Engineering, Beihang University, as a lecturer. He is currently undertaking research as a visiting researcher with the Department of Electronic and Electrical Engineering, University of Sheffield, Sheffield, U.K. He has now authored and co-authored more than 40 journal and conference publications. His current research interests include moving target detection, high-resolution spaceborne SAR image formation and three-dimensional imaging.

Jie Chen (M'06) received the B.S. and Ph.D. degrees in information and communication engineering from Beihang University (Beijing University of Aeronauticsand Astronautics, BUAA), Beijing, China, in 1996 and 2002, respectively. His Ph.D. study was focused on novel spaceborne synthetic aperture radar (SAR) system modeling and signal processing. From 2004, he was an associate professor with the School of Electronics and Information Engineering, Beihang University (BUAA). He was awarded New Century Excellent Talents in University, (NCET), by Ministry of Education, China, in 2006, and Excellent Young Teachers in University, by Fok Ying Tong Education Foundation and Ministry of Education, China, in 2008, respectively. He was a visiting researcher at the School of Mathematics and Statistics, University of Sheffield, Sheffield, UK, from 2009 to 2010, working with Prof. Shaun Quegan on ionospheric effects on low-frequency space radars that measure forest biomass and ionospheric electron densities. Dr. Chen is a full professor with the School of Electronics and Information Engineering, Beihang University (BUAA) from 2011. He has published more than 70 journal and conference papers, and he is the holder of 12 patents in the field of microwave remote sensing. His current research interests include multimodal remote sensing data fusion; topside ionosphere exploration with spaceborne HF/VHF-SAR system; high-resolution spaceborne SAR image formation and SAR image quality enhancement.

Wei Liu (S'01-M'04-SM'10) received the B.Sc. degree in space physics (minor in electronics) and the L.L.B. degree in intellectual property law from Peking University, Beijing, China, in 1996 and 1997, respectively; the M.Phil. degree in electrical and electronic engineering from The University of Hong Kong, Pokfulam, Hong Kong, in 2001; and the Ph.D. degree in electronics and computer science from the University of Southampton, Southampton, U.K., in 2003.
He was a Postdoctoral Researcher with the School of Electronics and Computer Science, University of Southampton, and later with the Communications and Signal Processing Group, Department of Electrical and Electronic Engineering, Imperial College London, London, U.K. Since September 2005, he has been a Lecturer with the Communications Research Group, Department of Electronic and Electrical Engineering, University of Sheffield, Sheffield, U.K. He has now authored and coauthored more than 140 journal and conference publications and a research monograph Wideband Beamforming: Concepts and Techniques (Wiley, 2010). His research interests are mainly in sensor array signal processing, blind signal processing, multirate signal processing, and their various applications in wireless communications, sonar, radar, satellite navigation, speech enhancement, and biomedical engineering.

Pengbo Wang received the Ph.D. degree in information and communication engineering from Beihang University (Beijing University of Aeronautics and Astronautics, BUAA), Beijing, China, in 2007. From 2007 to 2010, he worked as a postdoc in the School of Electronics and Information Engineering, Beihang University. From 2010 to 2013, he has been with the school of Electronics and Information Engineering, Beihang University (BUAA), as a lecturer. He was a visiting researcher at the Department of Electronic and Electrical Engineering, University of Sheffield from 2013 to 2014. He was an associate professor from 2015, and his current research interests include high-resolution spaceborne SAR image formation and multimodal remote sensing data fusion.